Time and Temperature Dependent Creep in Tournemire Shale

Z. Geng, A. Bonnelye, M. Chen, Y. Jin, P. Dick, C. David, X. Fang, A. Schubnel

To cite this version:

Z. Geng, A. Bonnelye, M. Chen, Y. Jin, P. Dick, et al.. Time and Temperature Dependent Creep in Tournemire Shale. Journal of Geophysical Research : Solid Earth, 2018, 123 (11), pp.9658-9675. 10.1029/2018JB016169 . hal-02881799

HAL Id: hal-02881799

https://hal.science/hal-02881799v1

Submitted on 7 Jul 2020

AGU100 ADVANCING EARTH AND SPACE SCIENCE

JGR

Journal of Geophysical Research: Solid Earth

RESEARCH ARTICLE

10.1029/2018JB016169

Key Points:

- Strengthening is observed during creep deformation of Tournemire shale
- A transition from pressure-solution compactive creep to brittle dilatant creep is observed
- Competition between microcrack growth, healing, and sealing accompanied by pressure solution process

Supporting Information:

- Supporting Information S1
- Data Set S1

Correspondence to:
Z. Geng,
zhi.geng@ens.fr

Citation:
Geng, Z., Bonnelye, A., Chen, M., Jin, Y., Dick, P., David, C., et al. (2018). Time and temperature dependent creep in Tournemire shale. *Journal of Geophysical Research: Solid Earth*, *123*, 9658–9675. https://doi.org/10.1029/2018JB016169

Received 4 JUN 2018
Accepted 10 NOV 2018
Accepted article online 15 NOV 2018
Published online 29 NOV 2018

Time and Temperature Dependent Creep in Tournemire Shale

Zhi Geng[1,2], **Audrey Bonnelye**[3], **Mian Chen**[2], **Yan Jin**[2], **Pierre Dick**[4], **Christian David**[5], **Xin Fang**[2], and **Alexandre Schubnel**[1]

[1]Laboratoire de Géologie de l'ENS (UMR 8538), PSL Research University, Paris, France, [2]State Key Laboratory of Petroleum Resources and Prospecting, China University of Petroleum, Beijing, China, [3]LMS, Ecole Polytechnique, CNRS, Université Paris-Saclay, Palaiseau, France, [4]Institut de Radioprotection et de Sûreté Nucléaire, Paris, France, [5]Département Géosciences et Environnement, Université de Cergy Pontoise, Cergy-Pontoise, France

Abstract We conducted a series of triaxial creep experiments on shale specimens coming from Tournemire, France, using the stress-stepping method up to failure, at a confining pressure of 80 MPa, on two orientations (parallel and perpendicular to bedding), and at temperatures of 26 and 75 °C. In these week-long experiments, stress, strains, and *P* wave ultrasonic velocities were recorded (quasi-) continuously. The strength at creep failure of Tournemire shale was ~70% higher than the peak strength measured during constant strain rate (~10^{-7}/s) experiments, and failure was reached at larger strains. An overall transition from *P* wave velocity increase at moderate differential stress to *P* wave velocity decrease closer to brittle failure was also observed. At a smaller timescale, *P* wave velocities initially decreased and then increased gradually during each step of creep deformation. The magnitude of these variations showed important (i) stress, (ii) orientation, and (iii) temperature dependences: larger increase was observed for *P* wave propagating along the main compressive stress orientation, larger decrease for *P* wave propagating perpendicular to it, and a changing behavior enhanced at a higher temperature. Scanning electron microscopy performed postmortem revealed evidence of time-dependent pressure solution, localized compaction, crack growth, and sealing/healing. Our data reveal that shale deformation is highly stress sensitive only in a narrow stress domain where stress corrosion cracking-induced brittle dilatant creep deformation is dominant. At stresses below, pressure solution compaction creep dominates the deformation and shales compact, consolidate, and heal. This has important implications for the mechanics of shallow fault zones and accretionary prisms.

1. Introduction

Time-dependent deformation mechanisms of upper crustal rocks have impacts on the brittle strength of rocks (Paterson & Wong, 2005), and thus on natural hazards such as earthquakes (Kanamori & Brodsky, 2004) or landslides (Terzaghi, 1951), and are of interest for the mechanics of oil and gas reservoirs (Anderson & Grew, 1977; Sone & Zoback, 2010) and long-term radioactive waste storage (Bonin, 1998). Under creep deformation conditions (constant stress), rocks may typically deform at very low strain rates (e.g., $<10^{-8}$/s), at the limit to what can be achieved practically in the laboratory. Traditionally, three stages of the creep curve (axial strain as a function of time) have conventionally been distinguished (see Figure 1): (1) primary or decelerating creep, (2) secondary or steady state creep, and in the specific context of brittle creep, (3) tertiary or accelerating creep to failure.

Brittle creep deformation, characterized by dilatancy eventually leading to failure, is typical of rocks being deformed under upper crustal conditions and has been observed in a number of lithologies including sandstone (Heap, Baud, Meredith, Bell, & Main, 2009; Ngwenya et al., 2001), basalt (Heap et al., 2011), borosilicate glass (Mallet et al., 2015), granite (Fujii et al., 1999), and limestone (Brantut et al., 2014). Brittle creep experimental studies have been recently reviewed by Brantut et al. (2013). During brittle creep, the strength is reduced compared to the peak strength observed during constant (higher) strain rate experiments on similar rock materials (Bhat et al., 2012; Bonnelye et al., 2017; Brantut et al., 2013; Peng & Podnieks, 1972) and the time to failure may increase from minutes to several years with decreasing applied stress. The dominant mechanism at play during brittle creep is subcritical crack growth (Brantut et al., 2013), a time-dependent process driven by stress corrosion (Anderson & Grew, 1977; Atkinson, 1979), which, before the onset of dilatancy, makes the strain rate extremely stress sensitive. By lowering the specific (Griffith) surface energy, water (either as porous fluid or adsorbed at the crack tips) promotes stress corrosion (Rice, 1978; Wong, 2000) and the resulting subcritical crack growth (Atkinson, 1984).

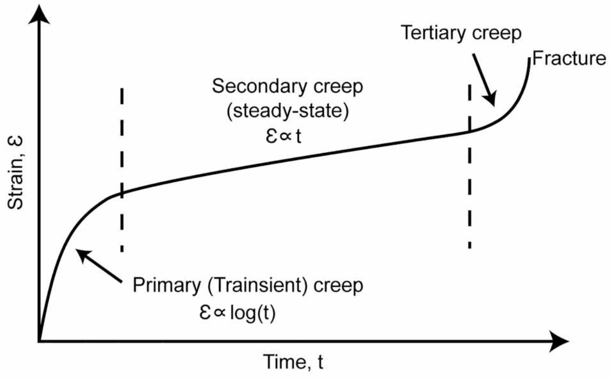

Figure 1. Illustration of brittle creep deformation under constant stress. (Modified from Scholz, 1968.)

In contrast to brittle creep, porous sedimentary rocks deformed in creep conditions at high pressure can also exhibit a compactive behavior (Heap et al., 2015; Nicolas, Fortin, Regnet, et al., 2017). The key difference between brittle creep and compaction creep is that in the latter case, the axial strain rate continuously decreases and brittle failure is never reached (Heap et al., 2015). For instance, Heap et al. (2015) observed the formation of compaction bands in Bleurswiller sandstones deformed in the compactant regime. In the case of sandstones, shear-enhanced compaction and the formation of compaction bands is also thought to be mainly driven by microcracking (Wong & Baud, 2012) and, in creep conditions, by subcritical crack growth (Heap et al., 2015). Compactive creep was also observed in limestones, but there, Nicolas, Fortin, Regnet, et al. (2017) observed a transition from compaction creep at low differential stresses, for which the strain rate exhibited a low-stress sensitivity, to brittle creep at higher differential stresses, where the strain rate became highly stress sensitive. They interpreted this transition as the deformation being dominated by intracrystalline plasticity at low stress/strain rates and by dilatant microcracking, eventually leading to failure, at higher stresses and strain rates.

Experiments conducted at room temperature and up to ~300 °C have also shown that pressure solution, a stress and temperature dependent mass transfer process, may also be a potential deformation mechanism during compaction creep (Brzesowsky et al., 2014; Gratier et al., 1999; Gratier et al., 2013; Pluymakers & Spiers, 2015; Zhang et al., 2010; Zhang & Spiers, 2005). In Crab Orchard sandstone deformed at 400 °C, Rutter and Mainprice (1978) showed that the dominant mechanism during creep deformation to be strain rate dependent, as they observed a transition from pressure-solution-driven creep for strain rates lower than 10^{-9}/s, to stress-corrosion-driven brittle creep at faster strain rates. Brantut et al. (2014) also observed a similar process in creep experiments on limestones at room temperature. In summary, creep deformation of rocks only refers to a specific type of stress conditions, at which, depending on the specific thermodynamic (pressure, stress, temperature, pH, water, and oxygen fugacity) intensive parameters, the deformation will kinetically be dominated by a specific deformation mechanism, for instance, pressure-solution, intracrystalline plasticity, or subcritical crack growth. Brantut et al. (2012) theoretically showed that the transition from pressure solution dominated creep to subcritical microcracking brittle creep should occur at increasing strain rates with increasing depth.

In the laboratory, the two limiting factors in performing creep deformation studies are time and the variability of natural samples cored from the same block of material. These are the main reasons why the stress-stepping methodology was developed (Gasc-Barbier et al., 2004) as an alternative to the more conventional method of constant stress loading. In the stress-stepping method, the axial differential stress is incrementally increased after the sample has deformed to a certain level (strain or time period). Tertiary creep and brittle failure are reached at the last stress increment only. Comparatively, the constant stress loading (or conventional creep method) produces complete information of creep deformation, while stress-stepping loading only generates primary and secondary creep curves. Gasc-Barbier et al. (2004) conducted creep experiments using both the conventional creep and the stress-stepping methods on shales coming from the Bure underground laboratory in France. Their short- (days) to long-term (2 years) investigations yielded an extensive understanding of the creep behavior of shales under low confining pressure. However, the stress-stepping approach is not only time-saving but also solves of the issue of samples variability, which becomes critical when studying a phenomenon so highly stress and temperature sensitive as subcritical crack growth. For instance, Heap, Baud, Meredith, Bell, and Main (2009) and Heap et al., 2011 demonstrated that the stress-stepping method successfully overcomes variability problem in Etna basalt and Darley Dale sandstone samples deformed under pressure up to 100 MPa and temperatures up to 75 °C. In both cases, deformation was dominated by subcritical crack growth, and axial strain rate was heavily sensitive to the applied differential stress.

The study of time-dependent deformation of shale might help to further understand shale deformation in the field. In general, the mechanical behavior of shale is strongly anisotropic (Bonnelye et al., 2017; Valès et al., 2004). Young's modulus in the direction parallel to bedding is higher than that the one perpendicular to bedding, the latter being more sensitive to confining pressure (Bonnelye et al., 2017). The failure of shale samples normally occurs in a brittle way, yielding a sudden collapse of strength (Su et al., 2017), but samples loaded parallel or normal to bedding reach failure at different strains, exhibit different strength, fracture angles, and strain rates (Naumann et al., 2007; Valès et al., 2004). Naumann et al. (2007) showed that the onset of dilatancy only occurred very close to the failure in Opalinus clay samples loaded normal to the bedding, which was also observed in Tournemire shale (Fabre & Pellet, 2006; Masri et al., 2014; Niandou et al., 1997; Valès et al., 2004). During creep deformation of shales such as Bure clay (Gasc-Barbier et al., 2004) or reservoir shale rocks such as Barnett, Haynesville, Eagle Ford, and Fort St. John shale (Sone & Zoback, 2014), the strain rates were shown to depend on the level of differential stress. Deforming a Tournemire shale sample normal to the bedding during multistage (similar to stress-stepping) uniaxial creep tests, Fabre and Pellet (2006) observed viscoplastic deformations with a considerable volumetric contraction during the secondary creep phase, followed by dilation close to failure. Geng et al. (2017) observed a surprisingly fast elastic anisotropy reversal observed during creep deformation of Tournemire samples deformed perpendicular to bedding.

In this study, we concentrate on the deformation mechanisms at play during creep in anisotropic Tournemire shale. We performed triaxial creep experiments using the stress-stepping method on samples of Tournemire shale, at confining pressure of 80 MPa, 25 and 75 °C, for two different orientations. Combining continuous mechanical and acoustic measurements, as well as microstructural observations, we demonstrate that the deformation of Tournemire shale is highly stress-sensitive only in a narrow stress domain where crack growth is dominant, and strain rate exceeds 10^{-8}/s. For stresses and resulting strain rates below 10^{-8}/s, pressure solution compaction creep dominates the deformation, and shales compact, consolidate, and heal.

2. Materials and Methods

2.1. Samples

The rock samples used in this study come from the underground laboratory of Institute of Radioprotection and Nuclear Safety (IRSN) located in Tournemire (southern France). Tournemire Shale is a Toarcian shale with low permeability (10^{-19} to 10^{-21} m^2) and a natural pore water content varying from 3.5 to 8% (Bonin, 1998; Masri et al., 2014). In the underground laboratory, the expected in situ stress is approximately 5 MPa. The average bulk density of samples is 2.57 (±0.06) g/cm^3, with a total porosity ranging from 6.5 to 10% (Boisson et al., 2001; Tremosa et al., 2012). The average composition (weight proportion) of this shale is 15–25% illite, 15–25% smectite and kaolinite, 10–30% calcite and dolomite, and 10–20% quartz (Bonin, 1998; Tremosa et al., 2012). A general understanding of the site in Tournemire and of the physical/mechanical properties of this argillaceous media are provided in Cabrera et al. (2001) and Valès et al. (2004). Cylindrical samples (diameter of 42 ± 1 mm) were cored in situ using air for cooling along two different bedding plane orientations (θ = 0° and 90° in Figure 2, where θ is defined as the angle between the bedding and the vertical). Samples used in this study were all cored away from the tunnel Excavation Damaged Zone (EDZ) in a relatively nonfractured area and were immediately placed within vacuum-sealed bags upon retrieval to avoid dehydration.

Previous to the experiments, samples were dry polished at both ends to a total length of 84.5 (±0.1) mm. As the dry polishing takes only 20 min, the dehydration effect is thought to be negligible in shales with such low permeability. Four pairs of strain gauges (four axial and four radial) were glued directly onto the cylindrical rock surface to provide local measurements of axial and the radial strains (denoted by R1 and R2 in Figure 2). We take compression as a positive and tension as a negative. The mean volumetric strain can be calculated by $\varepsilon_v = \overline{\varepsilon}_{\mathrm{axial}} + \overline{\varepsilon}_{\mathrm{R1}} + \overline{\varepsilon}_{\mathrm{R2}}$. Samples were then inserted into a rubber jacket perforated with 16 holes where *P* wave velocity transducers were glued. These transducers are made of piezoelectric ceramics sensitive to compressional *P* waves, with a center frequency close to 1 MHz (Boston Piezo PZT5A). Sensors network and strain gage disposition varied according to the bedding angle of samples, as shown in Figure 2.

2.2. Experimental Setup

The triaxial apparatus used in this study is an externally heated oil-medium confining triaxial cell, built by Sanchez Technologies and installed at Laboratoire de Géologie of ENS-Paris (France). Detailed description

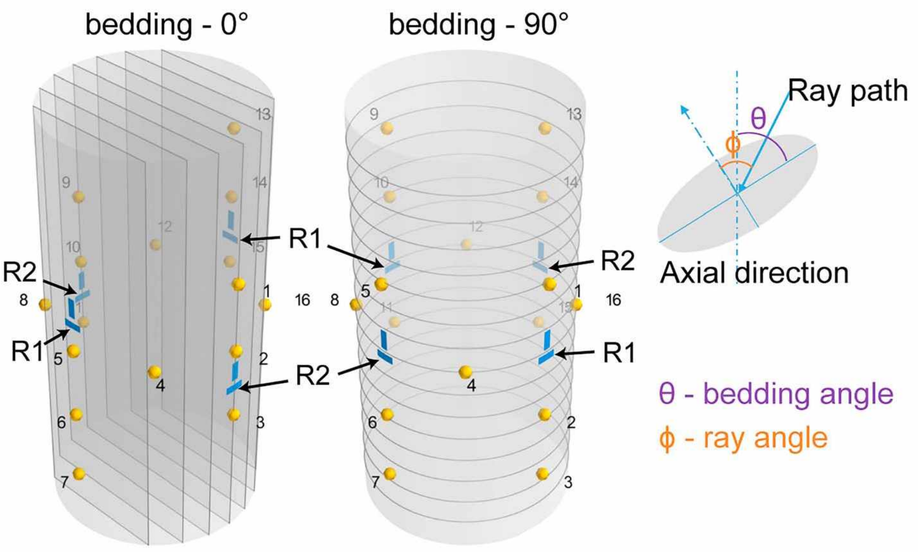

Figure 2. Schematics of the samples' orientation, instrumentation, and conventions on bedding angle (θ) and raypath direction angles (ϕ). The golden balls are *P* wave transducers; the blue rectangles are axial (vertical) and radial (horizontal) strain gauges (R1 and R2).

and a schematic view of this apparatus can be found in Brantut et al. (2011). Axial load and confining pressure are applied via two independent servo-controlled pumps, with controlling accuracy of the order of 10^{-3} MPa. Because of the extremely low permeability of shales, pore pressure is difficult to control during laboratory deformation experiments performed on relatively large samples. Here the pore pressure system was vented to ambient and in the following, we will assume that the deformation took place within the drained regime (i.e., constant and homogeneous pore pressure equal to 1 atm throughout the specimen). Three capacitive gap-sensors measure the total axial displacement of the piston externally during deformation. The averaged value of the three sensors was used to calculate axial strain, which was then corrected for machine stiffness (Brantut et al., 2011). Strains, displacements, and stress recordings were sampled at 0.5 Hz.

Acoustic transducers were connected inside the vessel using 50 Ohms coaxial cables to a 16-channel digital oscilloscope (Mini Richter System, ASC Ltd.) via 45 dB high-frequency preamplifiers. In the following, we refer to a *P* wave velocity survey as an ultrasonic monitoring procedure during which each channel is alternatively pulsed with a voltage of 500 V (1 μs risetime), while the 15 remaining transducers record the wavefield. Each survey thus results in a set of 16 × 15 ultrasonic waveforms, which are then stacked 10 times, in order to enhance the signal-to-noise ratio, and recorded at a sampling rate of 10 MHz. The characteristic duration of a survey is 30 s. While changing stress, surveys were performed every 5 min; under creep conditions, surveys were performed every 15 min.

2.3. *P* Wave Velocity Processing

During processing, the *P* wave arrival times of a reference master survey performed at hydrostatic conditions were manually picked. Other waveforms were then cross correlated relative to this reference survey, in order to get relative travel time differences. When performing cross correlations, waveforms were resampled to 50 MHz using a spline function, so that the cross-correlation resolution (i.e., time step) was 0.02 μs only. The cross-correlation method is described in Pettitt et al. (2002).

P wave velocities along each available raypath were then obtained from travel time and the distance between sensors that are considered constant throughout the experiment. Assuming the shale samples are homogeneous and transversely isotropic, we averaged velocities passing through the center of the specimen along raypath of similar orientations. The raypath angle ϕ (Figure 2) is defined as the angle between the raypath and the normal to the bedding plane. In the following, *P* wave velocities are thus measured and averaged relative to the normal of bedding (and not relative to the compression direction). Error on *P* wave velocities relative to sensor network distortion is lower than 1%, that is, comparable to the relative error between

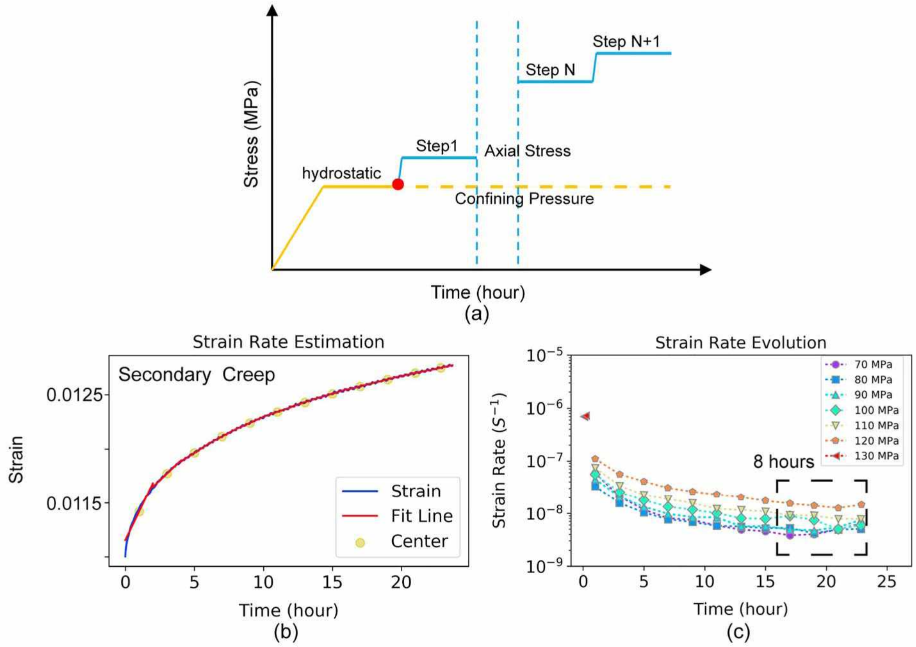

Figure 3. (a). Experimental loading procedure. (b) Illustration of creep strain rate estimates. Strain rate (s^{-1}) is calculated as the slope of each segments (red lines) over a 2-hr period of time (yellow dots). (c) Strain rate (s^{-1}) evolution of a sample deformed parallel to bedding, at various differential stress. The time interval used to estimate strain rate is 2 hr; the rectangle box indicates the period of 8 hr over which the strain rates presented in the following are calculated.

consecutive measures along a given raypath, and smaller than the absolute error which are regard as lower than 5%.

2.4. Stress-Stepping Methodology

Following Heap, Baud, Meredith, Bell, and Main (2009), we used the stress stepping methodology (Figure 3a). Samples were first loaded under hydrostatic conditions up to 80 MPa, at a pressure rate of 0.3 MPa/min. Hydrostatic conditions were maintained for ~18 hr, during which the vessel was heated at a rate of ~0.2 °C/min for tests conducted at 75 °C. Next, differential stress ($\sigma_1 - \sigma_3$) was increased to a fixed initial creep stress (Table 1), and kept constant (creep conditions) for 24 hr. Differential stress was repeatedly increased by 10 MPa and maintained constant for 24 hr, until the last step at the end of which brittle failure occurred. When increasing the differential stress, the loading rate was 0.5 MPa/min. Experimental conditions are summarized in Table 1. The term D' is the ratio between differential stress at the dilatant point and the peak strength (results from conventional triaxial experiments performed by Bonnelye et al. (2017) on the same core sampled in the tunnel), while the term Q' is the ratio between the first step of differential stress and the peak strength, listed for reference.

D' is the ratio between differential stress at the dilatant point and corresponding peak strength (results from conventional experiments conducted by Bonnelye et al., 2017). Q' is the ratio between initial differential stress used for creep and corresponding peak strength.

Table 1
Summary of Tested Experimental Conditions

Bedding angle (°)	Confining pressure (MPa)	Temperature (°C)	D'	Q'	Initial creep stress (MPa)	Stress step (MPa)
0	80	26	0.6	0.99	70	10
		75	-	-	70	10
90		26	0.8	0.56	60	10
		75	-	-	60	10

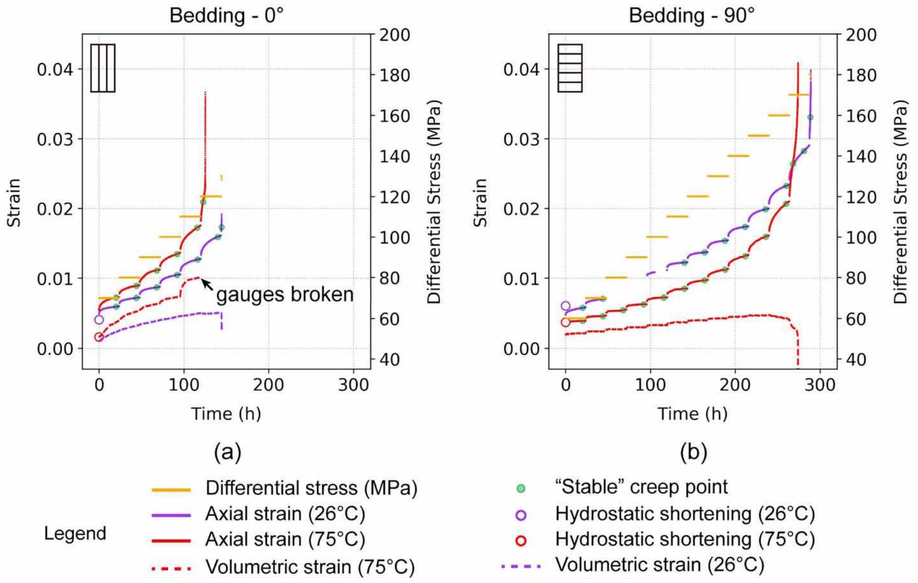

Figure 4. Creep curves of (a) 0° bedding samples and (b) 90° bedding samples, modified from Figure 1 of Geng et al. (2017). The missing sections of axial and volumetric strain curves (26 °C) in subfigure (b) resulted from technical issues with the recording system.

At each step of differential stress, the strain rate was calculated by fitting linearly axial strain data set over every period (e.g., 2 hr). This corresponds to the apparent strain rate over a given time period. Strain rate generally stabilized during the last 8 hr (Figure 3c). In the following, we used the average strain rate over the last 8 hr of each step to characterize the quasi-secondary creep strain rate under corresponding loading stress. Strain rate data are inevitably noisy (e.g., electromagnetic interference, transducer sensitivity, sampling error, and environmental temperature fluctuation), and the resolution is of the order of 4×10^{-9}/s (i.e., 10 μm shortening over an 8-hr period).

3. Results

3.1. Stress, Strai,n and Strain Rate

Strain and differential stress are plotted as a function of time in Figure 4, for the two bedding orientations tested, and for both room (26 °C) and high (75 °C) temperatures. Observed shortening during hydrostatic compression was systematically smaller at 75 °C than at 26 °C. Assuming the average thermal expansion coefficient of clay is 5×10^{-5}/°C (3.4×10^{-5}/°C by McTigue, 1986, and 6.3×10^{-5}/°C by Monfared et al., 2011), the volumetric thermal expansion due to an increase of 50 °C in temperature is approximately 2.5×10^{-3}, which is coherent with the average value measured ($2.6 \times 10^{-3} \pm 0.2 \times 10^{-3}$).As summarized in Table 2, for both orientations, room temperature and 75 °C samples failed at a higher stress level than the one observed on samples coming from the same coring campaign, deformed under the same confining pressure (80 MPa), at room temperature and constant strain rate (~10^{-7}/s) conditions. The *creep failure strength* observed here were closer but remained smaller than the peak strength observed at faster strain rate (~10^{-5}/s). The total shortening (or axial strain) reached before failure was larger during these stress-stepping experiments than during the constant strain rate experiments. The largest axial strain at failure was reached during high-

Table 2
Summary of Sample Strength and Axial Strain at Failure

Bedding angle	Creep at 26 °C	Creep at 75 °C	Const. strain rate ~10^{-7}/s	Const. strain rate 4×10^{-5}/s
0°	130 MPa	120 MPa	71 MPa	140.5 MPa
	0.019	0.037	0.009	0.021
90°	180 MPa	170 MPa	106.48 MPa	194.5 MPa
	0.040	0.040	0.032	0.027

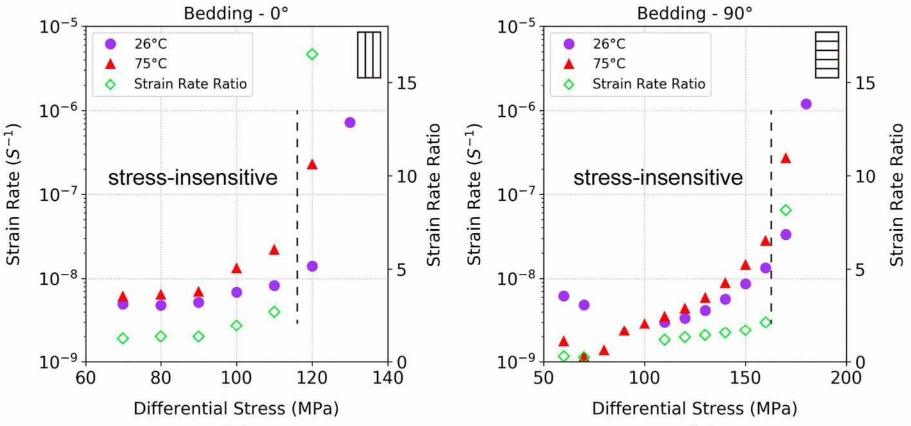

(a) (b)

Figure 5. Stress sensitivity of strain rates. (a) Samples loaded parallel to bedding. (b) Samples loaded perpendicular to bedding. The purple symbols are for room temperature samples, the red symbols are for 75 °C samples, and the open green symbols correspond to the strain rate ratio between high temperature and room temperature strain rates measured at a given differential stress.

temperature experiments (Figures 4a and 4b). A final observation is that the volumetric strain, when available, was never dilatant except during the very last stress steps.

The strength induced by constant strain rate deformation is from Bonnelye et al. (2017).

Strain rate evolutions are displayed in Figure 5 for both orientations and temperatures. One should first notice that strain rates during experiments at 75 °C were systematically faster than the ones measured at room temperature. Second, strain rates in shales exhibit little stress sensitivity; that is, for most stresses conditions tested, except for the final stages, it remained quasi-constant, with a slightly increasing trend with increasing stress. However, during the two to three final differential stress stages, the stress sensitivity increased significantly. Moreover, the temperature did not always enhance the creep strain rate at all differential stress steps. In Figure 5a, for 0° bedding samples, the creep strain rates at 75 °C were increasingly higher than the value at 26 °C. In contrast, for 90° bedding samples, the creep strain rates at 75 °C during the early period of deformation were lower than the value at 26 °C (Figure 5b), which might result from the larger initial hydrostatic compaction in the 90° bedding samples than in the 0° bedding samples (Figures 4a and 4b).

3.2. Evolution of *P* Wave Velocities

The evolution of *P* wave velocities as a function of strain is displayed in Figure 6. Samples deformed parallel to bedding (Figures 6a and 6b) show subtle variations in *P* wave velocities during deformation. First, the velocities measured under hydrostatic conditions at 75 °C were slower than the ones measured at room temperature, which is expected because of thermal expansion and the negative dependence of elastic moduli on temperature. Second, one can see that in both cases, velocities decreased during the initial part of differential loading and then increased during creep. In the latter stages of the experiments, the overall trend of velocities is to decrease. Overall, *P* wave anisotropy remained constant if not somewhat increased.

This behavior is better illustrated in Figures 7a and 7b, which shows Δv, the difference between the *P* wave velocities at a given time with that measured at hydrostatic conditions. Looking at Δv, one can see that the overall trend of velocities at different ray angles was to increase under low to moderate stress, then to decrease gradually approaching failure. Indeed, in each single stress step (see the zoom in in Figures 7a and 7b), most of the *P* wave velocities decrease during increasing differential stress (indicated by gray scatters) and primary creep stage, and then increase gradually during quasi-secondary creep. As the differential stress is getting larger and larger, the amount of velocity recovery diminishes, and the decrease becomes dominant. Again, the overall macroscopic behavior, as well as the behavior during each stress step, can be seen as a progressive transition between an increase in *P* wave velocity (stiffening) and a decrease of *P* wave velocity (weakening). Interestingly, as expected for crack growth in tri-axial conditions, the maximum velocity

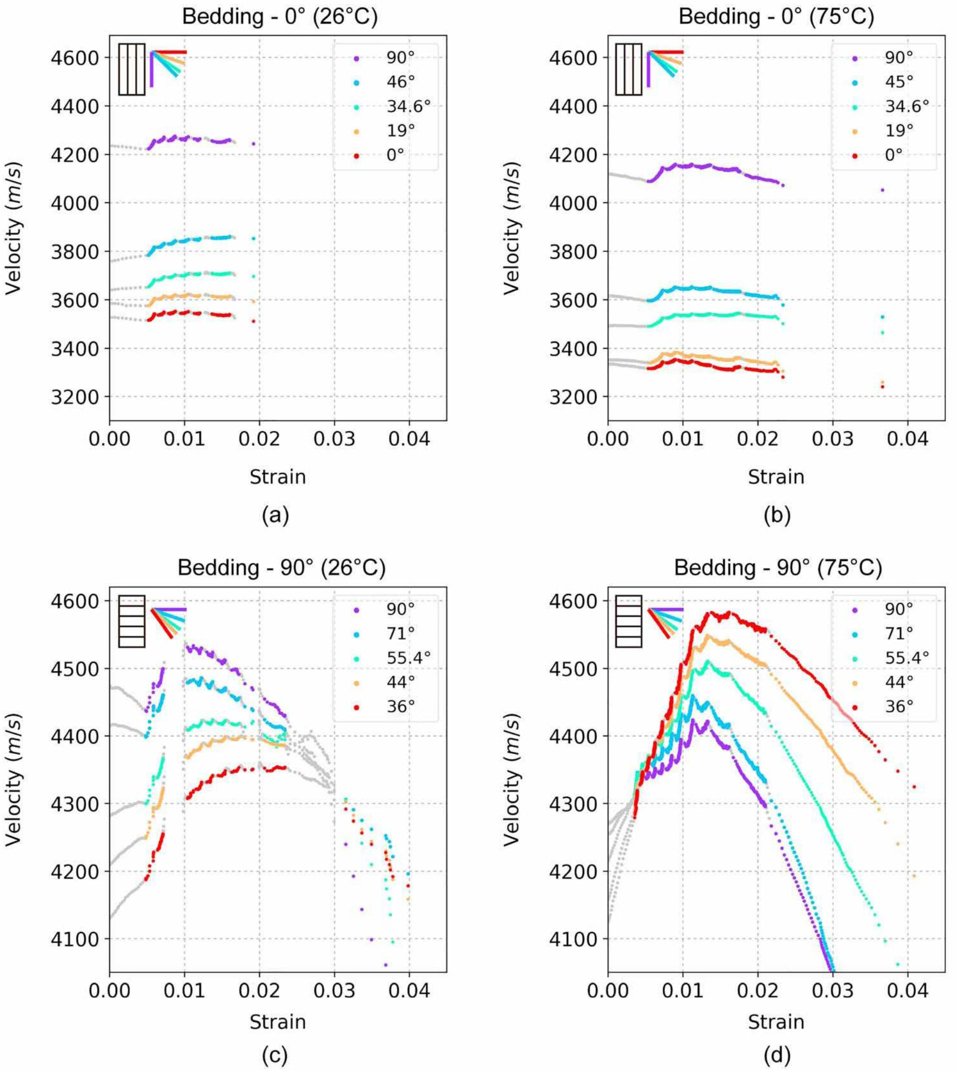

Figure 6. *P* wave velocities as a function of strain, orientation, temperature, and raypath angle (relative to the normal of bedding). (a and b) Samples deformed parallel to bedding at room temperature and 75 °C, respectively. (c and d) Samples deformed perpendicular to bedding at room temperature and 75 °C, respectively, modified from Figure 2 of Geng et al. (2017). The grey dots correspond to measurements performed during periods of increasing differential stress; the colored dots denote velocities measured under constant differential stress.

decrease was seen for waves propagating perpendicular to the main compressive axis (Schubnel & Guéguen, 2003). In contrast, waves propagating along raypaths (45° and 34.6°) closer to the main compressive axis showed a maximum increase.

P wave velocities measured in the samples deformed perpendicular to bedding (Figures 6c, 6d, 7c, and 7d) magnified the behavior mentioned above. The evolution of *P* wave velocities can be qualitatively discussed in the same manner as the samples deformed parallel to bedding. Velocities decreased during loading and primary creep stage, increased during quasi-secondary creep stage. The ratio of increase to decrease was greater under low to moderate stress conditions than the one under high stress, so that overall, stiffening was observed. The raypath dependence was similar, in that velocities measured along bedding, perpendicular to the main compressive stress exhibited larger decrease and smaller increase. Conversely, velocities measured closer to the main compressive axis (perpendicular to bedding) exhibited a larger increase and a smaller decrease. In contrast to the samples deformed parallel to bedding, this resulted in an overall convergence of *P* wave velocities and a decrease of *P* wave anisotropy. Anisotropy reversal was reached near failure at a strain of ~0.03 for the room temperature sample. At 75 °C, anisotropy reversal was reached at a strain of

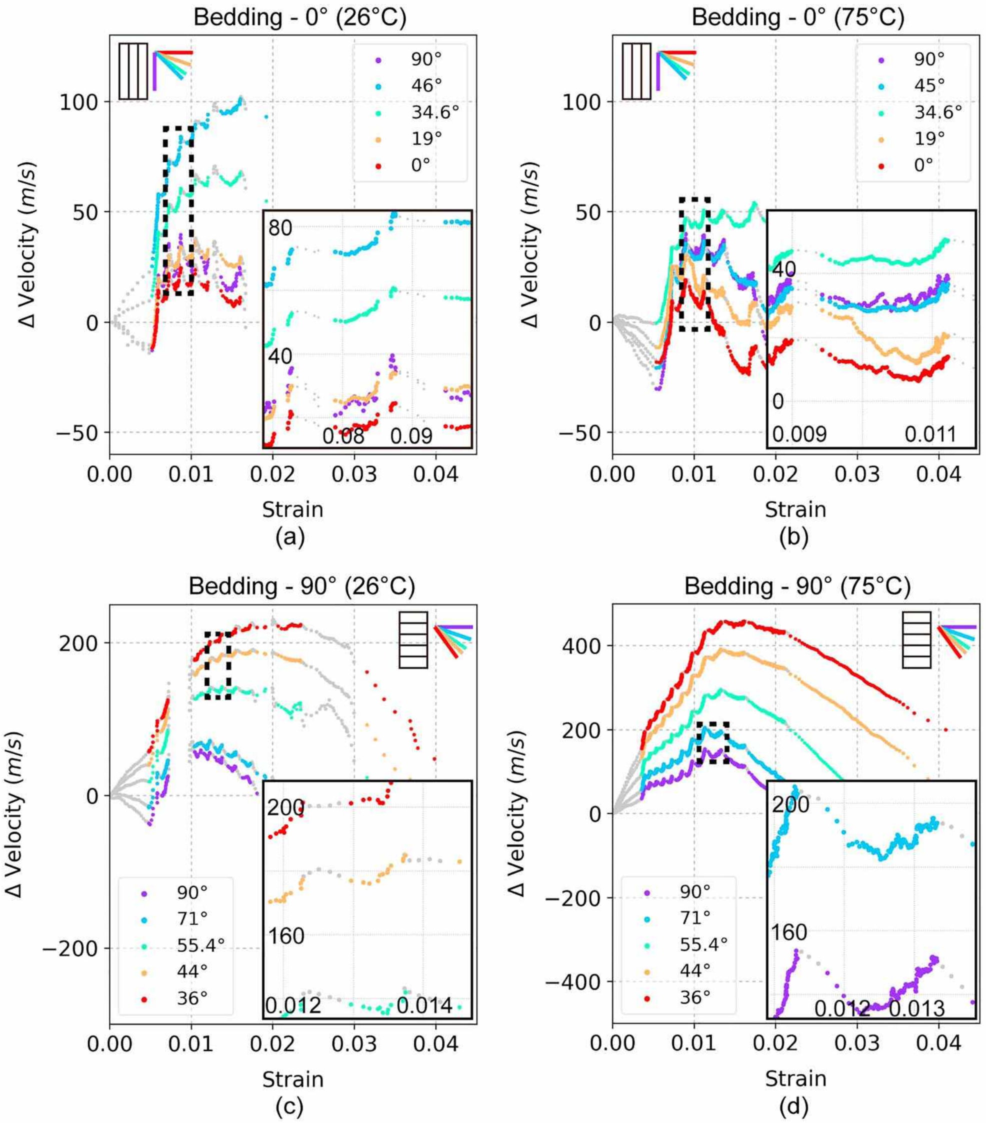

(a) (b)

(c) (d)

Figure 7. Relative velocities change as a function of strain. (a and b) Samples deformed parallel to bedding at room temperature and 75 °C respectively. (c and d) Samples deformed perpendicular to bedding at room temperature and 75 °C, respectively, modified from Figure 2 of Geng et al. (2017). The grey dots correspond to measurements performed during periods of increasing differential stress; the colored dots denote velocities measured under constant differential stress. The inset figures are zoomed to the same scale.

~0.006 only. Geng et al. (2017) already extensively discussed anisotropy reversal and its implications, so in this paper, we discuss it only briefly.

The time-dependent evolution of *P* wave velocities during creep deformation is highlighted in Figure 8. During each creep period of a sample deformed perpendicular to bedding, the average *P* wave velocities increased logarithmically with time. Under low to moderate stress, the average *P* wave velocity increased gradually throughout the creep period. However, at high stress, for example 140 MPa, the average *P* wave velocity first decrease during the primary creep stage (0–16 hr) and then increased. Note that during the quasi-secondary (steady state) creep stage (from 16 to 24 hr), the average velocities always increased at a rate, which approximately increased with elevating the stress levels from low to moderate loading stress.

3.3. Microstructural Observations

After each experiment, samples were impregnated in epoxy, dry-cut, polished, and finally carbon-coated for scanning electron microscopy (SEM) around macroscopic shear localization area. Crack sealing (filled with

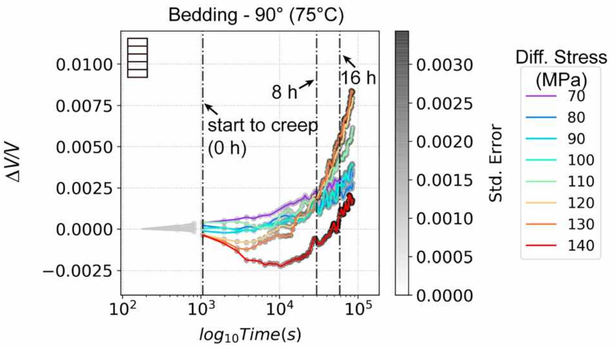

Figure 8. Time-dependent evolution of the average *P* wave velocity during creep deformation of the sample deformed perpendicular to bedding at 75 °C. The gray symbols indicate standard deviation of the velocity average. The color coding corresponds to differential stress.

introduced solid phases) and healing (merged together) were observed pervasively. In the 0° bedding sample (26 °C), a fracture subparallel to the axial stress is sealed (Figure 9a), and the walls appear to be healed (Figure 9b). At 75 °C, evidence for plastic flow is found in the sealing material or the matrix around fractures (denoted by the dashed lines in Figure 9 c and the arrow in Figure 9d). Sealed cracks were also found in both shear (Figure 9e) and tensile (Figure 9f) fractures in the 90° bedding sample (26 °C). Sealing/healing evidence may explain part of the increase both in velocities and strength during creep deformation.

More comprehensive microstructural investigations were performed on the sample deformed perpendicular to bedding at 75 °C. There, we observed substantial evidence of pressure solution. Localized porosity reduction is clearly evidenced along a fracture subparallel to bedding, highlighted by yellow dashed-lines (Figure 10a). Within the consolidation band, grains distribute more densely than in the area outside, and void space (marked in black) is almost absent. Figure 10d is a high-resolution magnification of the area marked by the red rectangle in Figure 10a, showing evidence of pressure solution at grain contacts. Grain contacts between dolomite grains are indented (yellow arrows), showing evidence of both dissolution and reprecipitation at merging grain boundaries. In comparison, grains outside the band distribute sparsely and were

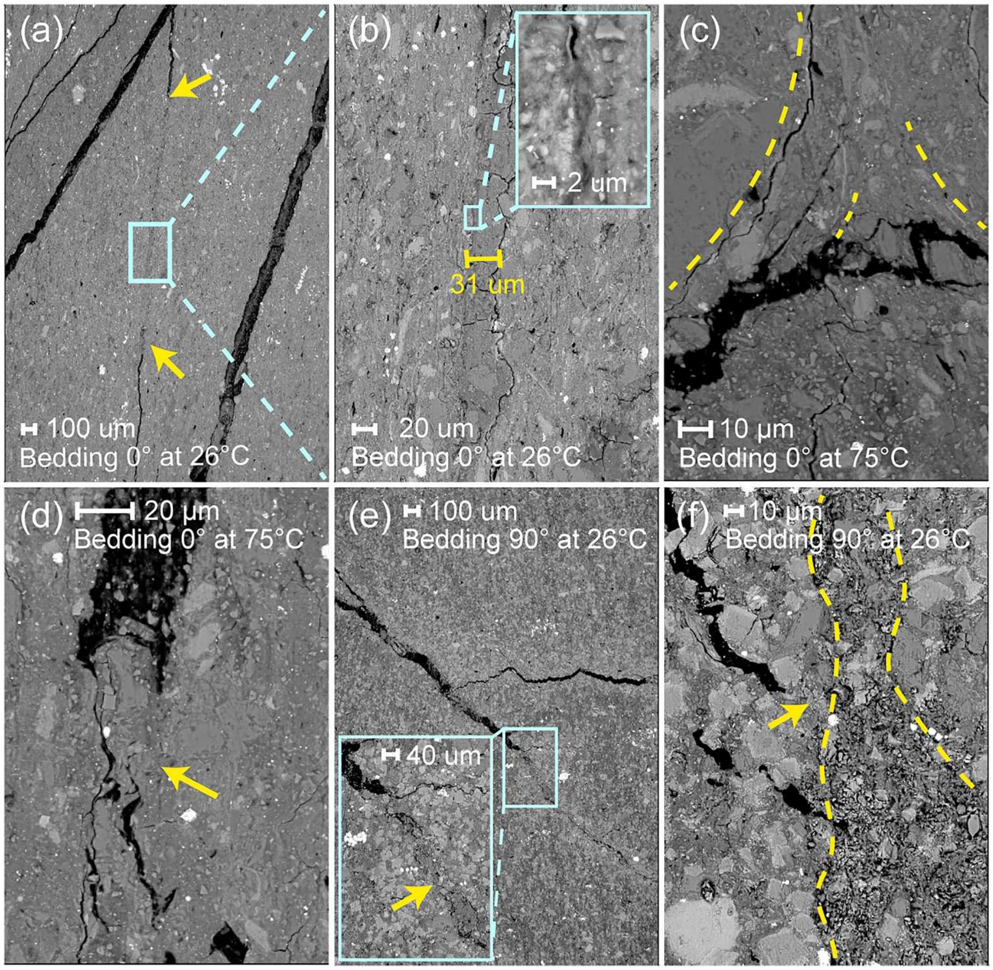

Figure 9. Cracks sealing/healing evidences in scanning electron microscopy images, taken using (a) 0° bedding samples (26°C) and (b) corresponding zoom figure of (a), (c and d) 0° bedding samples (75°C), and (e and f) 90° bedding samples (26 °C), after creep failure. The direction of axial stress is vertical.

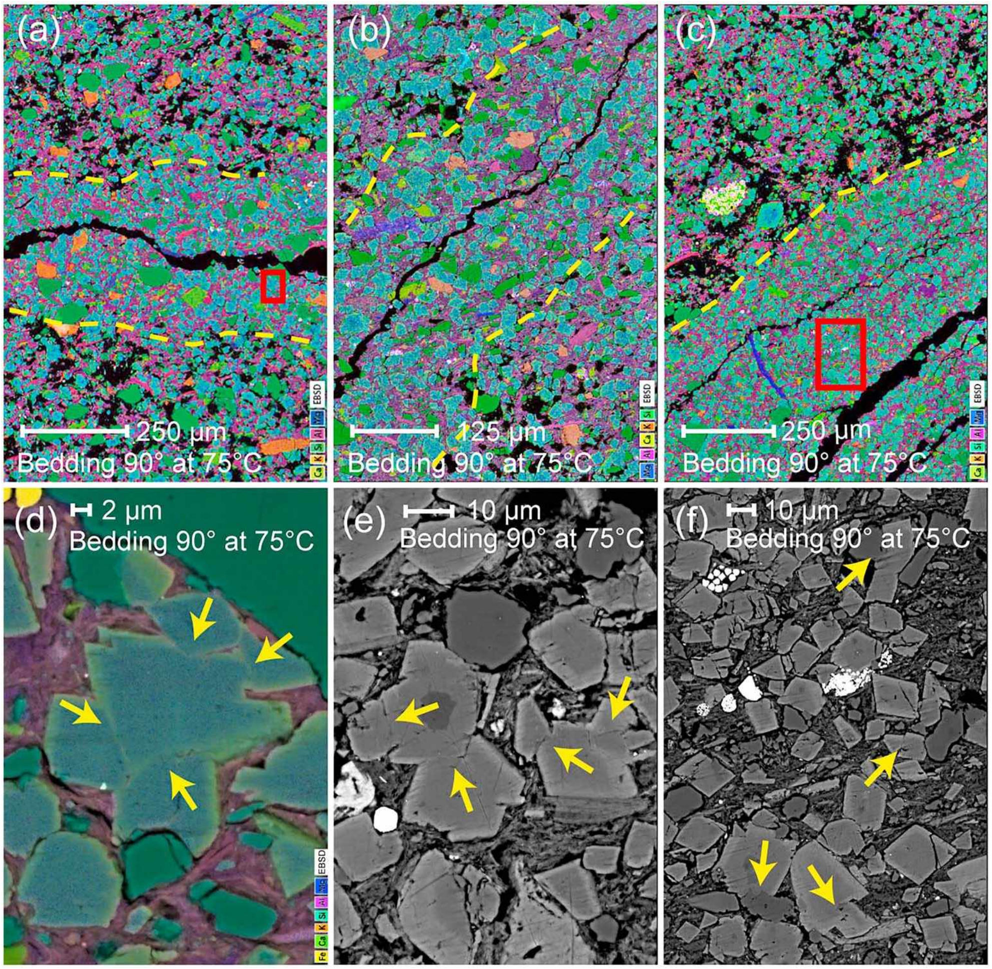

Figure 10. Pressure solution evidence in 90° bedding sample deformed at 75 °C. (a–d) Energy-dispersive spectroscopy (EDS) on scanning electron microscopy images. (e and f) Corresponding zoomed scanning electron microscopy images, denoted by the red rectangles in (b) and (c), respectively. The subfigure (e) is outside the scope of (b). In EDS images, light-green denotes calcite, dark-green indicates quartz, brown means feldspar, purple shows clay, and light-blue represents dolomite. The direction of axial stress is vertical. The subfigure (d) is an EDS version of the Figure 3f in Geng et al. (2017).

wrapped by clay (purple color in the matrix), without evidence of indentation. Similarly, localized consolidation was also observed along shear fractures (Figures 10b and 10c), with the corresponding pressure solution evidence within the band (Figures 10e and 10f). It seems that the fractures may have acted as preferential mass transfer channels along which localized creep compaction occurred, due to pressure solution active during deformation.

4. Discussion

4.1. Pressure Solution Creep Kinetics in Tournemire Shales

Our observations suggest that under low to moderate stresses, a plausible underlying mechanism of creep is intergranular pressure solution. Pluymakers and Spiers (2015) showed diffusion-controlled pressure solution as the controlling mechanism of grain-size dependent compaction creep in anhydrite fault gouge. Hellmann, Renders, et al. (2002) and Zhang et al. (2010) demonstrated that compaction creep was driven by pressure solution at upper crustal reservoir temperature in chalk (25–80 °C) and calcite powder (28–150 °C), respectively. For our Tournemire shale, in order to eliminate the apparent compaction resulting from grain rearrangement, microcracks, and bedding closure or sliding, we had precompacted the sample in hydrostatic pressure (80 MPa) for ~18 hr. Besides our deformation data, the microstructural images in Figure 10 clearly

Table 3
Parameters Used for Pressure-Solution Compaction Creep Kinetics

Parameters	Value	Note
V_s (mol/m^3)	6.43×10^{-5}	Molar volume of dolomite (Chichagov, 1994)
R (J/mol/K)	8.32	Gas constant
T (K)	299~348	Temperature
Dw (m^3/s)	3×10^{-18}	The product of diffusion coefficient and thickness of the grain boundary fluid film. (Zhang et al., 2010)
c (mol/m^3)	0.0076	Effective molar solubility of dolomite (est. from Aqion)
d (m)	1×10^{-5}	the grain size of dolomite

show evidence of pressure solution in the 90° bedding sample at 75 °C. Chemical mapping analysis indicated that the outermost shells of dolomite grains were enriched in iron (light yellow in Figure 10d and light grey in Figures 10e and 10f), possibly coming from clay minerals present in the rock matrix. On the stressed intergranular boundaries, the shell seems to have dissolved as denoted by arrows in Figures 10d–10f. In all the samples, we observed evident sealing or healing of cracks by clay minerals or fine-grain solid phases. Similar cemented areas in chalk were previously interpreted as precipitation phases and mass redistribution during pressure solution dominated deformation by Hellmann, Gaviglio, et al. (2002).

Pressure solution creep is generally expressed using exponential laws. Here we use the law for diffusion-limited pressure solution creep, published by Gratier et al. (2011):

$$\dot{\varepsilon} = 8DwcV_s\left(e^{3\Delta\sigma_n V_s/(RT)} - 1\right)/d^3 \tag{1}$$

where D is a diffusion coefficient of ions in the thin water film, w is the thickness of the grain boundary fluid film, c is the molar solubility of the diffusing solid, V_s is the molar volume of the stressed solid, R is a gas constant, T is the temperature in Kelvin, $\Delta\sigma_n$ is differential stress, and d is the grain size. In our experiments, $e^{3\Delta\sigma_n Vs/RT} \gg 1$, because the stresses are high, so that the above equation can be simplified to

$$\dot{\varepsilon} = Ae^{3\Delta\sigma_n V_s/RT} \tag{2}$$

where $A = 8DwcV_s/d^3$. Note that equation (2) becomes linear in semilog coordinate ($\log_{10}\dot{\varepsilon}$ vs. $\Delta\sigma_n$), with a slope that is 1.3 Vs/RT and an intercept equals to $\log_{10}(A)$.

Using a molar volume of $V_s = 6.45 \times 10^{-5}$ m^3/mol for dolomite (listed in Table 3), we find a slope of 0.028 and 0.033 (MPa^{-1}) at 75 °C and room temperature respectively, which is larger but within the same order of magnitude with the exponential stress sensitivity (slope) observed in our experiments at low to moderate stresses, which ranged between 0.0083 and 0.015 (MPa^{-1}) (see Figure 11). The discrepancy might arise from the fact that our samples contain 10–30% dolomite only.

Zhang et al. (2010) gave an estimation of Dw for calcite, ranging from 5.74×10^{-20} to 2.98×10^{-18} m^3/s between room temperature and 150 °C. On the other hand, Renard et al. (2000) modeled the kinetics of pressure solution process around an active fault, showing the timescale of pervasive pressure solution in the fine clay fault gouge to be much smaller than previously thought, because dissolution and diffusion are enhanced in the presence of clays. Here using the upper value for Dw, a solubility $c = 0.76 \times 10^{-3}$ mol/m^3, and a grain-size of 10 μm, we find a pressure solution accommodated strain rate of 2 to 3.35×10^{-8}/s at 100-MPa differential stress, which is compatible with our data. Similar estimation using data for quartz would yield pressure solution strain rates of the order of ~10^{-10}/s only, meaning that if the creep deformation is truly pressure solution dominated in our samples, it is due to carbonate/dolomite dissolution/reprecipitation, which is supported by our microstructural observations (Figure 10). Finally, the observed stress sensitivity and strain rates at higher stresses are both at least 1 order of magnitude larger than the one observed at lower to moderate stresses and thus difficult to explain using pressure solution creep.

4.2. Stress Corrosion Microcracking-Induced Brittle Dilatant Creep

It is generally accepted that brittle creep in sandstones, igneous rocks, and ceramics is driven by subcritical crack growth within grains and along grain boundaries (Brantut et al., 2013; Lawn, 1993). Here creep deformation became highly stress sensitive at higher stresses and our Tournemire shale samples underwent a transition to dilatant brittle creep, until failure. Creep deformation is generally expressed either in the form of a power law or an exponential law. The power law relation, most widely used for steady state brittle creep in rocks, is defined as (Charles, 1958)

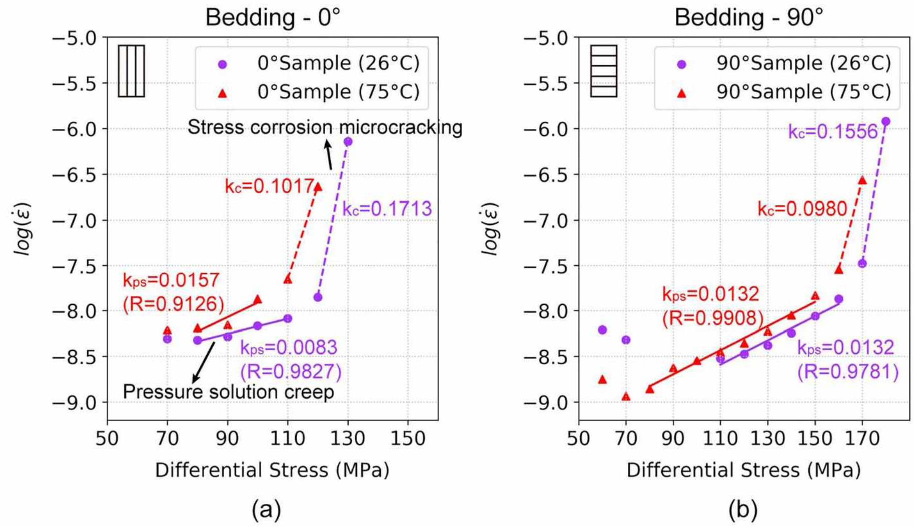

Figure 11. Stress sensitivity of creep in Tournemire shales, for samples deformed at pressure of 80 MPa, (a) parallel to bedding and (b) perpendicular to bedding, at room (purple dots) and 75 °C (red triangles). Strain rate data are fitted using an exponential-law model (equation (2)). k_{ps} is the slope indicating pressure solution creep, while k_c is the slope implying stress corrosion microcracking that is discussed in the text.

$$\dot{\varepsilon} = Ce^{\left(\frac{-Q_s}{RT}\right)}\sigma^n \tag{3}$$

where C (MPa^{-n}/s) is a material constant, Q_s (J/mol) is an activation energy, R is the gas constant, T is the temperature (K), and σ (MPa) is the differential stress. The stress exponent n generally has a characteristic value for a given deformation mechanism. For dislocation creep for instance, $n = 3$. For stress corrosion brittle creep, n is typically much larger (>10).

In our experiments, we find stress exponents n ranging from 27–37 at 75 °C to 49–63 at room temperature (Figure 12). In comparison, Heap, Baud, Meredith, Bell, and Main (2009) reported comparable stress exponents on various sandstones. The stress sensitivities of those sandstones were reduced to 19–54 at 75 °C, while ranged from 45.6 to 66.5 at room temperature. Our data are also comparable to that of Tavel limestone (Nicolas, Fortin, & Guéguen, et al., 2017), in the brittle dilatant creep regime (see Figure 12a). In contrast, Rybacki et al. (2017) presented secondary creep deformation in Posidonia shale (see Figure 12b) far before failure, indicating a stress exponent of only 0.975, which they interpreted as nondilatant dislocation creep. In summary, it means the dominant deformation mechanism active in our Tournemire samples close to the failure is compatible with previously published data on stress corrosion cracking in both quartz/clay aggregates and pure calcite samples, deformed under similar pressure-temperature conditions.

4.3. Strain Rate Dependence of Brittle Strength

The failure strength of Tournemire shale is much more sensitive to deformation rate than to temperature (see Figure 13a). Bonnelye et al. (2017) conducted conventional (constant strain rates) triaxial experiments at room temperature (26 °C) using the same material under the same confining pressure of 80 MPa. Here the failure strength of our samples exceeded by ~70% in average the strength obtained by Bonnelye et al. (2017) (Figure 13a) for 10^{-7}/s experiments. Note that except during tertiary creep stage, the strain rates in our experiments ranged between 10^{-9}/s and 10^{-8}/s, that is, 1 to 2 orders of magnitude smaller than that of Bonnelye et al. (2017). This is counterintuitive, because our general understanding of rock strength is that failure strength of brittle rocks deformed at a lower strain rate is smaller than the peak strength induced under a higher deformation rate (Bhat et al., 2012; Bonnelye et al., 2017; Brantut et al., 2013; Peng & Podnieks, 1972). The latter statement agrees with the observation of Bonnelye et al. (2017) that the peak strength of samples deformed at a constant strain rate of ~10^{-7}/s was significantly smaller than the strength resulting from the constant strain rate of ~10^{-5}/s (Figure 13a). Note that our stress-stepping creep experiments were conducted under a series of constant stresses, with corresponding strain rates ranging from

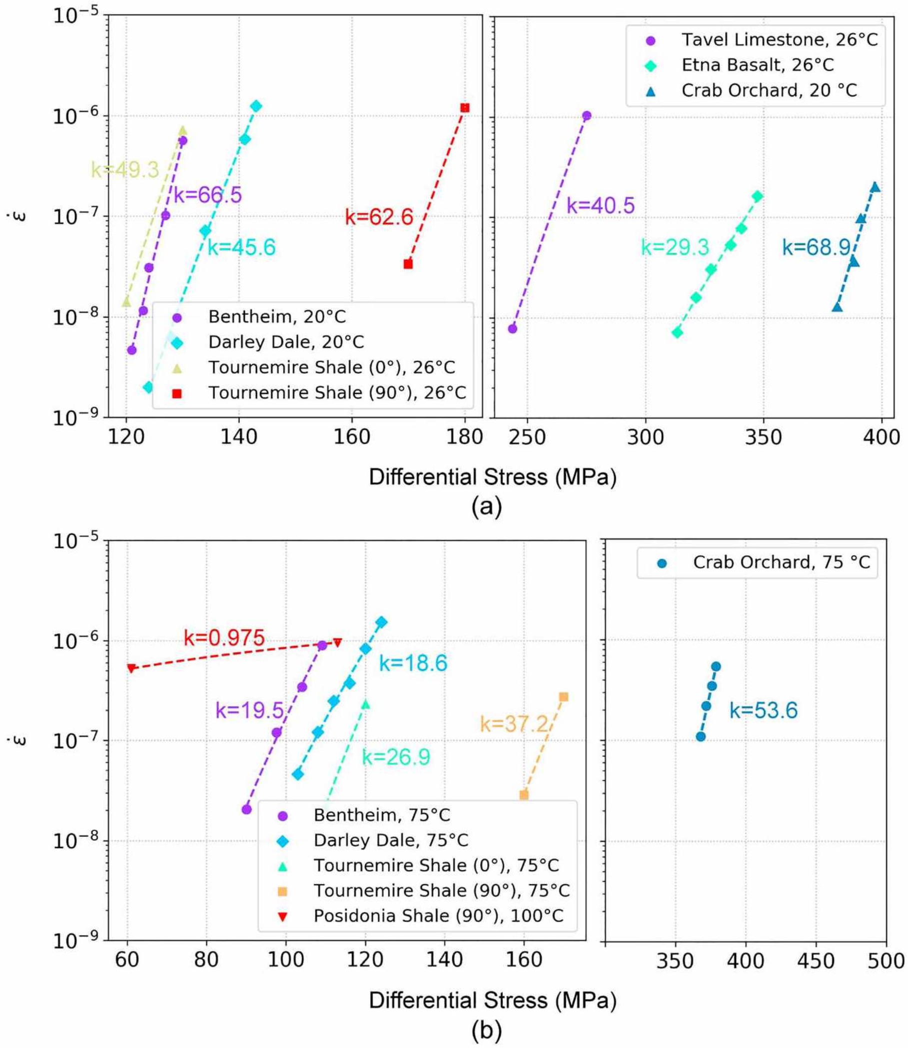

Figure 12. Brittle dilatant creep strain rate s in Tournemire shale compared with sandstone data (Bentheim, Crab Orchard, and Darley Dale) from Heap, Baud, Meredith, Bell, and Main (2009), at (a) room temperature and (b) 75 °C, and nondilatant creep data (100 °C) of Posidonia shale from Rybacki et al. (2017). Strain rate data are fitted using a power law model (equation (3)). *k* is the slope of fitted lines; the minimum correlation coefficient is 0.9871.

~10^{-9}/s to ~10^{-6}/s, which was associated with various deformation mechanisms. Because the reduction of porosity or damage contribute to the time-dependent recovery of velocities (Schubnel et al., 2005), both the recovery of acoustic velocities and microstructural observations confirmed sealing/healing of cracks, as well as the occurrence of pressure solution during week-long creep deformation under low to moderate stresses. Although these observations potentially explain the significant strengthening compared with constant strain rate experiments, it remains unclear at this point whether samples would have eventually failed under low to moderate stresses, if the stress condition had been kept constant.

A possible explanation of the bimodal strain rate dependence of brittle failure strength in Tournemire shale is illustrated in Figure 13b, where four different regimes of deformation are discussed (Figure 13a). At fast strain rate ($>10^{-5}$/s), in regime I, tensile cracks subparallel with maximum principal stress propagate over a short period of time. In low permeability rocks ($\ll 10^{-17}$ m^2) such as Tournemire shales, pore pressure cannot equilibrate, and accordingly, the pore pressure and effective stress will be respectively low and high at crack tips, which will inhibit crack propagation. This mechanism, generally referred to as *dilatancy hardening*, is dominant only when cracks propagate faster than pore pressure, even at the scale of the representative elementary volume. As such, it is a high-frequency (i.e., fast deformation rate) regime, which in pluri-centimetric

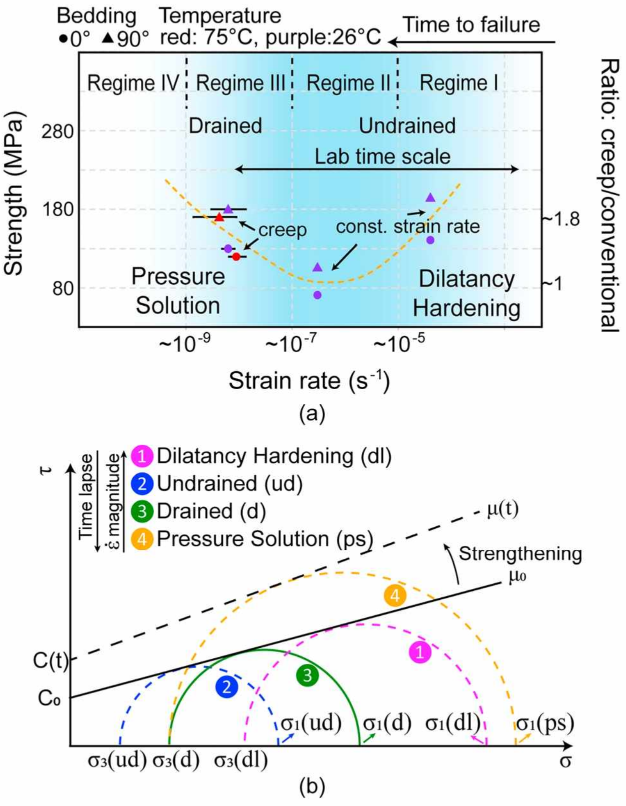

Figure 13. A conceptual model of strain rate -dependent brittle strength of Tournemire shale. (a) Regime classification of strain rate and corresponding mechanism for failure strength. The points around the constant strain rate of 10^{-7}/s and 10^{-5}/s are from Bonnelye et al. (2017), at 26 °C. (b) Illustration of the strain rate-dependent strength of brittle failure.μ_0 indicates a laboratory coefficient of internal friction (short-term), while $\mu(t)$ represents a time-dependent coefficient of internal friction (long-term).

shales specimen, seems to be attained for strain rates $\gg 10^{-5}$/s, in which case, the strength increases and the Mohr-Coulomb circle would be displaced to the right (circle 1 in Figure 13b).

Regime II corresponds to the undrained case, where pore pressure has time to equilibrate in the representative elementary volume and the fluid mass is kept constant. Regime III represents the drained case, where pore pressure is now constant and the pore fluid has time to flow in and out the sample. The transition between the two regimes depends on the diffusion length, which is either larger or smaller than the specimen length L. Duda and Renner (2012) proposed that the critical strain rate above which the experiments are performed under undrained conditions is given by

$$\dot{\varepsilon}_{cr} = \frac{0.1 D \varepsilon_f}{l^2} \qquad (4)$$

where l is the sample length, ε_f is the strain at failure, and D is the hydraulic diffusivity. D is related to the permeability in the following manner: $D = k/\gamma\beta\phi$, where β is the fluid compressibility (5×10^{-10} Pa^{-1} for water) and ϕ is the porosity. For $k{\sim}10^{-20}$ m^2 as reported for Tournemire shales (Matray et al., 2007), a strain at failure of 0.05, a porosity of 10%, and a sample length of 0.08 m, the critical strain rate above which deformation remains undrained is 4×10^{-7}/s, which is comparable to the low strain rates of Bonnelye et al. (2017). Under high stress and pressure, one can expect the permeability of samples to be even lower, so that, at a strain rate of ${\sim}10^{-7}$/s Bonnelye et al. (2017) argued that the samples were deformed in the undrained regime, although the pore pressure system was vented at both ends. Because the effective stress is expected to be lower in undrained than in drained conditions, the Mohr circle is now shifted to the left (smaller failure strength, circle 2 in Figure 13b).

Finally, the last regime corresponds to strain rate for which pressure solution creep is expected ($\lesssim 10^{-9}$/s). In this last case, the rock is expected to consolidate over time so that the strength will increase due to increasing cohesion, and the Mohr-Coulomb failure envelope will be shifted to higher shear stresses (dashed line in Figure 13b). In this long-term (years) deformation regime, the laboratory Mohr-Coulomb failure criteria (solid line in Figure 13b) established using (relatively fast) constant strain rate experiments is not valid anymore and a time-dependent evolution of the cohesion is needed, as illustrated by the dash line in Figure 13b.

5. Implications and Conclusions

In sandstones, compaction creep is generally characterized by a reduction in porosity and a gradual deceleration in axial strain rate (Heap et al., 2015), which was active during the early period of stress-stepping creep deformation. This is not the case here, as creep deformation results from the balance between subcritical stress corrosion cracking and pressure solution, as predicted by Brantut et al. (2012). A direct proof of this is the decrease of velocities at the beginning of each creep section under low to moderate stress loading, followed by a velocity increase, which slows down to a steady value, while strain rate decelerates to an apparent constant value. This might have implications at the scale of fault zones, where elastic wave velocity recovery has been observed immediately after earthquakes (Brenguier et al., 2008; Schaff & Beroza, 2004). This recovery of elastic properties in shallow fault zones, dominated by clay mineralogy, over timescales of a couple of weeks, might be due to strain rate variations during the postseismic phase and pressure solution creep. Elastic anisotropy also reversed rapidly in the 90° bedding sample deformed at 75 °C, which potentially also has important implications for local stress rotation observed near active faults (Faulkner et al., 2006; Healy, 2008), as already discussed by Geng et al. (2017). Our laboratory data suggest that P wave anisotropy can evolve rather rapidly both over short time and space scales. At the field scale, continuous monitoring of fast

P wave direction and anisotropy at lower frequencies near fault zones over monthly timescales may help us decipher the state of stress on the fault.

Out of the diversity of microstructural observations, we have mainly discussed the pressure solution. Our observations of sealing and healing during creep deformation might also have implications on the time-dependent behavior of fault gouge. In fault zones, newly formed gouge will compact, seal, and heal as a function of time when fault motion ceases (Pluymakers & Spiers, 2015). Scholz and Engelder (1976) argued that creep deformation could increase asperity contact area of material and cause healing. In consequence, the actual strength of fault might actually depend on both its interseismic strain rate and the average inter-event time. For instance, a fault creeping fast will exhibit little seismicity and will remain relatively weak, whereas a fault locked might be stronger.

On the other hand, one consequence of this work is to demonstrate that brittle strength measurements of shaly fault cores in the laboratory probably give little indication on the actual mechanical strength of these materials at geological timescales and in situ conditions. The creep failure strength of our samples increased by nearly 70% compared to the conventional peak strength obtained by Bonnelye et al. (2017). We showed that poroplastic materials like shales are extremely strain rate dependent, and their dependence can be classified intro into four strain regimes: dilatancy hardening, undrained condition, drained status, and pressure-solution strengthening with decreasing strain rates, respectively. Creep deformation of our shale samples was also greatly influenced by temperature. In general, an increase of temperature results in a substantial increase of stress corrosion, and thus of the creep strain rate (Heap, Baud, & Meredith, et al., 2009; Kranz et al., 1982; Zhang et al., 2010). This turns to be more complex when pressure solution is active, because there, the stress sensitivity arises from a Boltzmann type exponential dependence, so that while strain rates were faster at 75 °C, we also observed a decrease of the stress sensitivity with increasing temperature. Interestingly, the compilation of brittle creep data in Figure 12 also shows a similar decrease of stress sensitivity of stress corrosion cracking with temperature, although overall, strain rates at given stress are faster. This could be expected from an exponential Boltzmann type dependence of stress corrosion cracking, rather than the power law expression used here in equation (3).

Finally, our results also have some implications on the mechanical behavior of sedimentary basin. Indeed, our observations of consolidation bands and compactive shear bands in clay material are, to our knowledge, the first consolidation bands observed not driven by microcracking (Heap et al., 2015; Wong & Baud, 2012), but rather by pressure solution processes. This is an interesting observation which ought to be delved deeper into, because in natural compaction bands observed in sandstones, grains are usually intact (Mollema & Antonellini, 1996), so that the consolidation bands described in our study maybe have more in common with natural compaction bands than what had been previously observed in the laboratory.

Acknowledgments
This research was funded by the National Natural Science Foundation of China (major program 51490651 and 51774305) and by the European Research Council grant ERC-2015-CoG: 681346 - REALISM. We are grateful to Damien Deldicque for microscopy imaging support at ENS and to IRSN for technical support providing samples. The data produced during our experiments are available in the supporting information.

References

Anderson, O. L., & Grew, P. C. (1977). Stress corrosion theory of crack propagation with applications to geophysics. *Reviews of Geophysics*, *15*(1), 77–104. https://doi.org/10.1029/RG015i001p00077

Atkinson, B. K. (1979). A fracture mechanics study of subcritical tensile cracking of quartz in wet environments. *Pure and Applied Geophysics*, *117*(5), 1011–1024. https://doi.org/10.1007/BF00876082

Atkinson, B. K. (1984). Subcritical crack growth in geological materials. *Journal of Geophysical Research*, *89*(B6), 4077–4114. https://doi.org/10.1029/JB089iB06p04077

Bhat, H. S., Rosakis, A. J., & Sammis, C. G. (2012). A micromechanics based constitutive model for brittle failure at high strain rates. *Journal of Applied Mechanics*, *79*(3), 12.

Boisson, J.-Y., Bertrand, L., Heitz, J.-F., & Golvan, Y. (2001). In situ and laboratory investigations of fluid flow through an argillaceous formation at different scales of space and time, Tournemire tunnel, southern France. *Hydrogeology Journal*, *9*(1), 108–123.

Bonin, B. (1998). Deep geological disposal in argillaceous formations: Studies at the Tournemire test site. *Journal of Contaminant Hydrology*, *35*(1-3), 315–330. https://doi.org/10.1016/S0169-7722(98)00132-6

Bonnelye, A., Schubnel, A., David, C., Henry, P., Guglielmi, Y., Gout, C., Fauchille, A. L., et al. (2017). Strength anisotropy of shales deformed under uppermost-crustal conditions. *Journal of Geophysical Research: Solid Earth*, *122*, 110–129. https://doi.org/10.1002/2016JB013040

Brantut, N., Baud, P., Heap, M., & Meredith, P. (2012). Micromechanics of brittle creep in rocks. *Journal of Geophysical Research*, *117*, B08412. https://doi.org/10.1029/2012JB009299

Brantut, N., Heap, M., Meredith, P., & Baud, P. (2013). Time-dependent cracking and brittle creep in crustal rocks: A review. *Journal of Structural Geology*, *52*, 17–43. https://doi.org/10.1016/j.jsg.2013.03.007

Brantut, N., Heap, M. J., Baud, P., & Meredith, P. G. (2014). Mechanisms of time-dependent deformation in porous limestone. *Journal of Geophysical Research: Solid Earth*, *119*, 5444–5463. https://doi.org/10.1002/2014JB011186

Brantut, N., Schubnel, A., & Guéguen, Y. (2011). Damage and rupture dynamics at the brittle-ductile transition: The case of gypsum. *Journal of Geophysical Research*, *116*, B01404. https://doi.org/10.1029/2010JB007675

Brenguier, F., Campillo, M., Hadziioannou, C., Shapiro, N., Nadeau, R. M., & Larose, E. (2008). Postseismic relaxation along the San Andreas fault at Parkfield from continuous seismological observations. *Science*, *321*(5895), 1478–1481. https://doi.org/10.1126/science.1160943

Brzesowsky, R., Hangx, S., Brantut, N., & Spiers, C. (2014). Compaction creep of sands due to time-dependent grain failure: Effects of chemical environment, applied stress, and grain size. *Journal of Geophysical Research: Solid Earth*, *119*, 7521–7541. https://doi.org/10.1002/2014JB011277

Cabrera, J., Beaucaire, C., Bruno, G., De Windt, L., Genty, A., Ramambasoa, N., et al. (2001). Projet Tournemire–Synthèse des programmes de recherche 1995–1999, Report# IPSN DPRE/SERGD, 01–19.

Charles, R. (1958). Static fatigue of glass. I. *Journal of Applied Physics*, *29*(11), 1549–1553. https://doi.org/10.1063/1.1722991

Chichagov, A. (1994). Information-calculating system on crystal structure data of minerals (MINCRYST), paper presented at Materials Science Forum, Trans Tech Publ.

Duda, M., & Renner, J. (2012). The weakening effect of water on the brittle failure strength of sandstone. *Geophysical Journal International*, *192*(3), 1091–1108.

Fabre, G., & Pellet, F. (2006). Creep and time-dependent damage in argillaceous rocks. *International Journal of Rock Mechanics and Mining Sciences*, *43*(6), 950–960.

Faulkner, D., Mitchell, T., Healy, D., & Heap, M. (2006). Slip on 'weak' faults by the rotation of regional stress in the fracture damage zone. *Nature*, *444*(7121), 922–925. https://doi.org/10.1038/nature05353

Fujii, Y., Kiyama, T., Ishijima, Y., & Kodama, J. (1999). Circumferential strain behavior during creep tests of brittle rocks. *International Journal of Rock Mechanics and Mining Sciences*, *36*(3), 323–337. https://doi.org/10.1016/S0148-9062(99)00024-8

Gasc-Barbier, M., Chanchole, S., & Bérest, P. (2004). Creep behavior of Bure clayey rock. *Applied Clay Science*, *26*(1-4), 449–458. https://doi.org/10.1016/j.clay.2003.12.030

Geng, Z., Bonnelye, A., Chen, M., Jin, Y., Dick, P., David, C., Fang, X., et al. (2017). Elastic anisotropy reversal during brittle creep in shale. *Geophysical Research Letters*, *44*, 10,887–810,895. https://doi.org/10.1002/2017GL074555

Gratier, J. R., Renard, F., Mittempergher, S., Doan, M. L., Toro, G. D., Hadizadeh, J., & Boullier, A. M. (2011). Aseismic sliding of active faults by pressure solution creep: Evidence from the San Andreas Fault Observatory at Depth. *Geology*, *39*(12), 1131–1134. https://doi.org/10.1130/G32073.1

Gratier, J.-P., Dysthe, D. K., & Renard, F. (2013). The role of pressure solution creep in the ductility of the Earth's upper crust. *Advances in Geophysics*, *54*, 47–179. https://doi.org/10.1016/B978-0-12-380940-7.00002-0

Gratier, J.-P., Renard, F., & Labaume, P. (1999). How pressure solution creep and fracturing processes interact in the upper crust to make it behave in both a brittle and viscous manner. *Journal of Structural Geology*, *21*(8-9), 1189–1197. https://doi.org/10.1016/S0191-8141(99)00035-8

Healy, D. (2008). Damage patterns, stress rotations and pore fluid pressures in strike-slip fault zones. *Journal of Geophysical Research*, *113*, B12407. https://doi.org/10.1029/2008JB005655

Heap, M. J., Baud, P., Meredith, P., Bell, A., & Main, I. (2009). Time-dependent brittle creep in Darley Dale sandstone. *Journal of Geophysical Research*, *114*, B07203. https://doi.org/10.1029/2008JB006212

Heap, M. J., Baud, P., Meredith, P., Vinciguerra, S., Bell, A., & Main, I. (2011). Brittle creep in basalt and its application to time-dependent volcano deformation. *Earth and Planetary Science Letters*, *307*(1-2), 71–82. https://doi.org/10.1016/j.epsl.2011.04.035

Heap, M. J., Baud, P., & Meredith, P. G. (2009). Influence of temperature on brittle creep in sandstones. *Geophysical Research Letters*, *36*, L19305. https://doi.org/10.1029/2009GL039373

Heap, M. J., Brantut, N., Baud, P., & Meredith, P. G. (2015). Time-dependent compaction band formation in sandstone. *Journal of Geophysical Research: Solid Earth*, *120*, 4808–4830. https://doi.org/10.1002/2015JB012022

Hellmann, R., Gaviglio, P., Renders, P. J. N., Gratier, J.-P., & Adler, P. (2002). Experimental pressure solution compaction of chalk in aqueous solutions. Part 2. Deformation examined by SEM, porosimetry, synthetic permeability, and X-ray computerized tomography. *Water-Rock Interactions, Ore Deposits, and Environmental Geochemistry: A Tribute to David A. Crerar*, *7*, 153–178.

Hellmann, R., Renders, P. J., Gratier, J.-P., & Guiguet, R. (2002). Experimental pressure solution compaction of chalk in aqueous solutions Part 1. Deformation behavior and chemistry.

Kanamori, H., & Brodsky, E. E. (2004). The physics of earthquakes. *Reports on Progress in Physics*, *67*(8), 1429–1496. https://doi.org/10.1088/0034-4885/67/8/R03

Kranz, R. L., Harris, W. J., & Carter, N. L. (1982). Static fatigue of granite at 200 C. *Geophysical Research Letters*, *9*(1), 1–4. https://doi.org/10.1029/GL009i001p00001

Lawn, B. R. (1993). *Fracture of brittle solids*, (Second ed.). Cambridge: Cambridge University Press.

Mallet, C., Fortin, J., Guéguen, Y., & Bouyer, F. (2015). Brittle creep and subcritical crack propagation in glass submitted to triaxial conditions. *Journal of Geophysical Research: Solid Earth*, *120*, 879–893. https://doi.org/10.1002/2014JB011231

Masri, M., Sibai, M., Shao, J.-F., & Mainguy, M. (2014). Experimental investigation of the effect of temperature on the mechanical behavior of Tournemire shale. *International Journal of Rock Mechanics and Mining Sciences*, *70*, 185–191. https://doi.org/10.1016/j.ijrmms.2014.05.007

Matray, J. M., Savoye, S., & Cabrera, J. (2007). Desaturation and structure relationships around drifts excavated in the well-compacted Tournemire's argillite (Aveyron, France). *Engineering Geology*, *90*(1–2), 1–16. https://doi.org/10.1016/j.enggeo.2006.09.021

McTigue, D. (1986). Thermoelastic response of fluid-saturated porous rock. *Journal of Geophysical Research*, *91*(B9), 9533–9542. https://doi.org/10.1029/JB091iB09p09533

Mollema, P., & Antonellini, M. (1996). Compaction bands: A structural analog for anti-mode I cracks in aeolian sandstone. *Tectonophysics*, *267*(1–4), 209–228. https://doi.org/10.1016/S0040-1951(96)00098-4

Monfared, M., Sulem, J., Delage, P., & Mohajerani, M. (2011). A laboratory investigation on thermal properties of the Opalinus claystone. *Rock Mechanics and Rock Engineering*, *44*(6), 735–747. https://doi.org/10.1007/s00603-011-0171-4

Naumann, M., Hunsche, U., & Schulze, O. (2007). Experimental investigations on anisotropy in dilatancy, failure and creep of Opalinus Clay. *Physics and Chemistry of the Earth, Parts A/B/C*, *32*(8-14), 889–895.

Ngwenya, B. T., Main, I. G., & Elphick, S. C. (2001). A constitutive law for low-temperature creep. *Journal of Geophysical Research*, *106*(B10), 21,811–821,826. https://doi.org/10.1029/2001JB000403

Niandou, H., Shao, J., Henry, J., & Fourmaintraux, D. (1997). Laboratory investigation of the mechanical behaviour of Tournemire shale. *International Journal of Rock Mechanics and Mining Sciences*, *34*(1), 3–16. https://doi.org/10.1016/S1365-1609(97)80029-9

Nicolas, A., Fortin, J., & Guéguen, Y. (2017). Micromechanical constitutive model for low-temperature constant strain rate deformation of limestones in the brittle and semi-brittle regime. *Geophysical Journal International*, *211*(1), 300–321. https://doi.org/10.1093/gji/ggx299

Nicolas, A., Fortin, J., Regnet, J., Verberne, B., Plümper, O., Dimanov, A., Spiers, C., et al. (2017). Brittle and semi-brittle creep of Tavel limestone deformed at room temperature. *Journal of Geophysical Research: Solid Earth*, *122*, 4436–4459. https://doi.org/10.1002/2016JB013557

Paterson, M. S., & Wong, T.-f. (2005). *Experimental rock deformation—The brittle field*. New York: Springer Science & Business Media.

Peng, S., & Podnieks, E. (1972). Relaxation and the behavior of failed rock, paper presented at International Journal of Rock Mechanics and Mining Sciences & Geomechanics Abstracts, Elsevier.

Pettitt, W. S., Baker, C., Young, R. P., Dahlström, L.-O., & Ramqvist, G. (2002). The assessment of damage around critical engineering structures using induced seismicity and ultrasonic techniques. In *The mechanism of induced seismicity*, edited, (pp. 179–195). Berlin: Springer.

Pluymakers, A., & Spiers, C. (2015). Compaction creep of simulated anhydrite fault gouge by pressure solution: Theory v. experiments and implications for fault sealing. *Geological Society, London, Special Publications*, *409*(1), 107–124. https://doi.org/10.1144/SP409.6

Renard, F., Gratier, J.-P., & Jamtveit, B. (2000). Kinetics of crack-sealing, intergranular pressure solution, and compaction around active faults. *Journal of Structural Geology*, *22*(10), 1395–1407. https://doi.org/10.1016/S0191-8141(00)00064-X

Rice, J. (1978). Thermodynamics of the quasi-static growth of Griffith cracks. *Journal of the Mechanics and Physics of Solids*, *26*(2), 61–78. https://doi.org/10.1016/0022-5096(78)90014-5

Rutter, E., & Mainprice, D. (1978). The effect of water on stress relaxation of faulted and unfaulted sandstone. *Pure and Applied Geophysics*, *116*(4–5), 634–654. https://doi.org/10.1007/BF00876530

Rybacki, E., Herrmann, J., Wirth, R., & Dresen, G. (2017). Creep of posidonia shale at elevated pressure and temperature. *Rock Mechanics and Rock Engineering*, *50*(B4), 1–20.

Schaff, D. P., & Beroza, G. C. (2004). Coseismic and postseismic velocity changes measured by repeating earthquakes. *Journal of Geophysical Research*, *109*, B10302. https://doi.org/10.1029/2004JB003011

Scholz, C. H. (1968). Mechanism of creep in brittle rock. *Journal of Geophysical Research*, *73*(10), 3295–3302. https://doi.org/10.1029/JB073i010p03295

Scholz, C. H., & Engelder, J. T. (1976). The role of asperity indentation and ploughing in rock friction—I: Asperity creep and stick-slip. *International Journal of Rock Mechanics and Mining Science and Geomechanics Abstracts*, *13*(5), 149–154. https://doi.org/10.1016/0148-9062(76)90819-6

Schubnel, A., Fortin, J., Burlini, L., & Gueguen, Y. (2005). Damage and recovery of calcite rocks deformed in the cataclastic regime. *Geological Society of London, Special Publications*, *245*(1), 203–221.

Schubnel, A., & Guéguen, Y. (2003). Dispersion and anisotropy of elastic waves in cracked rocks. *Journal of Geophysical Research*, *108*(B2), 2101. https://doi.org/10.1029/2002JB001824

Sone, H., & Zoback, M. (2010). Strength, creep and frictional properties of gas shale reservoir rocks, paper presented at 44th US Rock Mechanics Symposium and 5th US-Canada Rock Mechanics Symposium, American Rock Mechanics Association.

Sone, H., & Zoback, M. D. (2014). Time-dependent deformation of shale gas reservoir rocks and its long-term effect on the in situ state of stress. *International Journal of Rock Mechanics and Mining Sciences*, *69*, 120–132. https://doi.org/10.1016/j.ijrmms.2014.04.002

Su, X., Nguyen, S., Haghighat, E., Pietruszczak, S., Labrie, D., Barnichon, J. D., & Abdi, H. (2017). Characterizing the mechanical behaviour of the Tournemire argillite. *Geological Society of London, Special Publications*, *443*(1), 97–113.

Terzaghi, K. (1951). *Mechanism of landslides*. Cambridge, Mass: Harvard University, Department of Engineering.

Tremosa, J., Arcos, D., Matray, J., Bensenouci, F., Gaucher, E. C., Tournassat, C., & Hadi, J. (2012). Geochemical characterization and modelling of the Toarcian/Domerian porewater at the Tournemire underground research laboratory. *Applied Geochemistry*, *27*(7), 1417–1431. https://doi.org/10.1016/j.apgeochem.2012.01.005

Valès, F., Minh, D. N., Gharbi, H., & Rejeb, A. (2004). Experimental study of the influence of the degree of saturation on physical and mechanical properties in Tournemire shale (France). *Applied Clay Science*, *26*(1-4), 197–207. https://doi.org/10.1016/j.clay.2003.12.032

Wong, T.-f. (2000). Failure mode and weakening effect of water on sandstone. *Journal of Geophysical Research*, *105*(B7), 16,371–16,389. https://doi.org/10.1029/2000JB900087

Wong, T.-f., & Baud, P. (2012). The brittle-ductile transition in porous rock: A review. *Journal of Structural Geology*, *44*, 25–53. https://doi.org/10.1016/j.jsg.2012.07.010

Zhang, X., & Spiers, C. J. (2005). Compaction of granular calcite by pressure solution at room temperature and effects of pore fluid chemistry. *International Journal of Rock Mechanics and Mining Sciences*, *42*(7-8), 950–960. https://doi.org/10.1016/j.ijrmms.2005.05.017

Zhang, X., Spiers, C. J., & Peach, C. J. (2010). Compaction creep of wet granular calcite by pressure solution at 28°C to 150°C. *Journal of Geophysical Research*, *115*, B09217. https://doi.org/10.1029/2008JB005853